A. Lacarelle[1]
e-mail: arnaud.lacarelle@tu-berlin.de

T. Faustmann

Institut für Strömungsmechanik
und Technische Akustik,
Technische Universität Berlin,
Müller-Breslau-Strasse 8,
10623 Berlin, Germany

D. Greenblatt

Faculty of Mechanical Engineering,
Technion-Israel Institute of Technology,
Technion City, Haifa 32000, Israel

C. O. Paschereit

O. Lehmann

D. M. Luchtenburg

B. R. Noack

Institut für Strömungsmechanik
und Technische Akustik,
Technische Universität Berlin,
Müller-Breslau-Strasse 8,
10623 Berlin, Germany

Spatiotemporal Characterization of a Conical Swirler Flow Field Under Strong Forcing

In this study, a spatiotemporal characterization of forced and unforced flows of a conical swirler is performed based on particle image velocimetry (PIV) and laser Doppler anemometry (LDA). The measurements are performed at a Reynolds number of 33,000 and a swirl number of 0.71. Axisymmetric forcing is applied to approximate the effects of thermoacoustic instabilities on the flow field at the burner inlet and outlet. The actuation frequencies are set at the natural flow frequency (Strouhal number $St_f \approx 0.92$) and two higher frequencies ($St_f \approx 1.3$ and 1.55) that are not harmonically related to the natural frequency. Phase-averaged measurement are used as a first step to visualize the coherent flow structures. Second, proper orthogonal decomposition (POD) is applied to the PIV data to characterize the effect of the actuation on the fluctuating flow. Measurements indicate a typical natural flow instability of helical nature in the unforced case. The associated induced pressure and flow oscillations travel upstream to the swirler inlet where generally fuel is injected. This observation is of critical importance with respect to the stability of the combustion. Harmonic actuation at different frequencies and amplitudes does not affect the mean velocity profile at the outlet, while the coherent velocity fluctuations are strongly influenced at both the inlet and outlet. On one hand, the dominant helical mode is replaced by an axisymmetric vortex ring if the flow is forced at the natural flow frequency. On the other hand, the natural flow frequency prevails at the outlet under forcing at higher frequencies and POD analysis indicates that the helical structure is still present. The presented results give new insight into the flow dynamics of a swirling flow burner under strong forcing. [DOI: 10.1115/1.2982139]

Keywords: swirling flows, PIV, LDA, POD, coherent structures, flow instability, flow forcing

1 Introduction

For the past decades, lean premixed combustion has become a standard feature in gas turbine engines and is expected to be implemented in aircraft engines. The main advantage of this combustion technique is that the low fuel/air ratio results in a lower burning temperature and produces relatively low NO_x emissions. One of the main disadvantages of lean premixed combustion is that it is susceptible to combustion instabilities that produce large-amplitude pressure oscillations that can damage the combustor and turbine. The mechanisms leading to thermoacoustic instabilities are numerous and closely related to each other: fuel/air ratio oscillations [1], acoustics boundary conditions [2], and flame surface oscillations induced by coherent structures [3,4].

These coherent flow structures are present in most combustors (jet flames, bluff body, and swirling flows) and lead to periodical oscillations of the velocity and mixing profile. This results in oscillations of the flame, which can excite acoustic modes of the combustor and in turn generate combustion instabilities. Particularly in swirling combustors, different coherent structures have been identified in experimental and numerical studies of isothermal flows [5–10]. Most of these investigations revealed a precessing vortex core (PVC) and a helical mode. The typical frequencies of these two phenomena were generally not related but some investigations showed that the frequency of the PVC was very closed or equal to the frequency of the helical mode [7] and par-

ticularly in a downscaled model of the burner used in this investigation [10]. In the shear layer of the flow, Kelvin–Helmholtz instabilities have also been observed [3,5,9]. The influence of the burner geometry, swirl number, expansion ratio, and boundary conditions on the flow field have also been investigated by many authors [11–13].

To avoid combustion instabilities induced by coherent structures, it is essential to understand their generation mechanism, as well as their evolution in the case of forced flows. The forcing, which is applied in the current investigation, approximates the impact of axial acoustic modes of combustion instabilities on the flow field in the burner.

Numerous experimental investigations on the excitation of simple jets have been reported in literature [14,15]. The forcing of those jets with different excitation modes generated axisymmetric or helical structures. Literature dealing with the experimental forcing of swirling jets is rare, and even rarer are studies carried out on swirl burners. One of the main reasons is that actuators may not have sufficient authority to excite the flow with an amplitude that is comparable to the oscillation amplitude that is attained under full-scale operating conditions ($\pm 10\%$ of the mean flow velocity).

Nevertheless, Paschereit et al. [3] investigated the flow in reacting and non-reacting flows on a model premixed burner. They observed that axisymmetrical and helical modes could be excited by changing the boundary conditions downstream of the combustion chamber. Cold flow investigations of the same burner in a water test rig showed that the helical mode found in the reacting experiments corresponded to a helical mode of the burner flow. Using the same burner type, Lacarelle et al. [16] showed that forcing at the frequency of the helical mode led to an increase in scalar mixing at the burner outlet. Phase-averaged measurements

from PIV data showed that axial forcing at the natural flow frequency replaced a helical mode with an axisymmetric mode at the burner outlet. Khalil et al. [17] also investigated the impact of forcing on the flow field of a generic swirler. They found that forcing frequency and amplitude have an influence on both the vortex shedding and mean-field of the flow. Pulsing at the natural flow frequency caused the development of axisymmetric vortex rings in the shear layer, while the unforced flow showed a $m=+2$ helical structure. Forcing at frequencies lower than two times the natural frequency resulted in a lock-in phenomenon of the vortex shedding frequency on the excitation, which disappeared for higher frequencies. The amplitude of the excitation had a significant impact on the breakdown position, which moved downstream as the amplitude increased.

As it is difficult to experimentally actuate the flow at a high amplitude over a wide frequency range, numerical simulations are often employed as these actuation boundary conditions can be relatively easily implemented. Wang and Yang [9] performed a large-eddy-simulation (LES) of the axially forced flow of a swirl injector with radial entry. They focused on forcing frequencies remaining below or equal to the natural flow frequencies of the PVC (4 kHz). One simulation was performed at the natural frequency of the shear layer (13 kHz). The amplitude of forcing was set to 10%. They showed that the forced axial disturbance may be split into two parts at the burner outlet: The propagation of the waves in the streamwise direction followed an acoustic wave, propagating at the speed of sound. On the other hand, the azimuthal oscillations were convected downstream with the local flow velocity. The excitation of the flow had a small impact on the mean flow properties, except when the forcing was applied at a frequency matching the natural flow frequency of the outer shear layer region. In this case mixing was dramatically enhanced.

The goal of this work is to understand the impact of strong forcing on the flow field at the inlet and outlet of a swirl burner. This is achieved by initially studying the unforced natural burner flow field and then comparing this to the forced case. Two measurement techniques (PIV and laser Doppler anemometry (LDA)) and postprocessing tools (phase averaging and proper orthogonal decomposition (POD)) are combined to characterize the unforced and forced flows. In Sec. 2, the experimental setup (water test rig with excitation mechanism) is presented. Then the measurement technique and the postprocessing tools used are described. Section 4 shows the results obtained with PIV and LDA at the burner outlet and inlet for the unforced flow of the burner. A typical helical structure is observed in this case and a physical explanation of the observed phenomenon is advanced. Section 5 focuses on the impact of axial forcing on the flow field at the inlet and outlet of the burner. Two excitation frequencies are chosen and show remarkable properties concerning the flow structures. The POD analysis of the PIV snapshots presented in Sec. 6 reveals the shape of the dominant structures for all forcing cases investigated, and a sensitivity analysis of the number of PIV snapshots needed to resolve the modes is shown. The results demonstrate the effectiveness of POD for the analysis of complex turbulent flows.

2 Experimental Setup

2.1 The Burner. The burner that is employed in this investigation is a full-size conical swirler, normally used in gas turbine engines. It consists of two halves of a cone that are shifted with respect to each other in the radial direction, such that two inlet slots of constant width are formed. The diameter of each cone-half at the outlet is $D=82$ mm. This diameter is used as a reference length for all characteristic numbers.

The airflow through the lateral slots generates a strong azimuthal velocity component. This component produces a flow with a high degree of swirl, which results in vortex breakdown near the burner outlet followed by a recirculation zone where the flame stabilizes. The recirculation of hot combustion gas, inside the flame, leads to a second oxidation and to a reduction in carbon
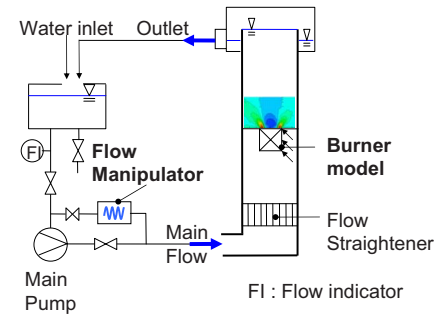

Fig. 1 Principle sketch of the water test rig illustrating the excitation mechanism

monoxide gas. The disadvantages of this type of flame stabilization are flow instabilities and complex three-dimensional coherent structures. A detailed description of the burner under running conditions is presented by Sattelmayer et al. [18] or Döbbeling et al. [19].

2.2 The Test Rig. The conical swirler was mounted in the square test section of a specially designed water test rig, which allows for full optical access to the burner from all four sides (see Fig. 1). The burner was secured to a plate, and this assembly was mounted in the center of the test section. The dump plane thus created had an expansion ratio burner/test section of 0.033.

The water test rig volume flow was set to 7.75 m³/h, which corresponds to a Reynolds number of 33,000. One of the main features of the test rig was the forcing mechanism, which was located upstream of the test section, in the bypass of the pump. It consisted simply of a standard rotating valve driven by an electric motor. Depending on the parameters set (valve position, volume flow, and frequency of forcing and rotation of the pump), strong forcing amplitudes were achievable (up to ±90% for some configurations). All the measurement points chosen exhibited an almost sinusoidal excitation, which could be acquired using a hydrophone (Bruel & Kjaer, type 8103) that was fixed on the burner outlet above slot S1 as shown in Fig. 2 (center of hydrophone located at $x/D=0.05$). The hydrophone was used to synchronize the triggering of the measurement equipment described below. A second hydrophone was also used to determine the rotational sense of the natural coherent structure.

The first PIV measurements made in planes containing the streamwise axis x for different burner angles θ showed that the flow at the burner outlet was not fully rotational symmetric, which can be explained by the lack of rotational symmetry of the burner geometry. The reference plane for the measurement was thus cho-
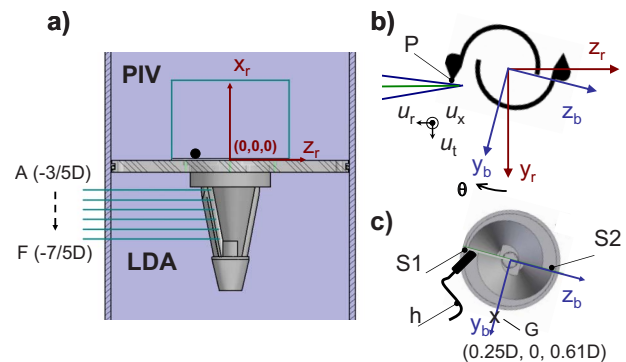

Fig. 2 Mounted burner in the test rig, side (a) and top views ((b) and (c)). The figures show the PIV and LDA measurement positions. S1 and S2 are the two slots of the burner. The hydrophone h was fixed on S1. For the LDA measurement in the slot, the angle θ was set equal to −20 deg.

sen to be the axial plane containing the two injection slots (x_b, z_b). With this definition and the two velocity components (u_x, u_t) (i.e., the streamwise and azimuthal components) recorded by the LDA at the burner exit $(x/D=0.25)$, it was possible to obtain an evaluation of the degree of swirl at the outlet. In our case, the swirl number S is defined as the ratio of azimuthal to streamwise momentum from $z=0$ to $z_s=50$ mm

$$S = \frac{2\pi \int_0^{z_s} \rho \bar{u}_x \cdot \bar{u}_t z^2 \cdot dz}{z_s \cdot 2\pi \int_0^{z_s} \rho \bar{u}_x^2 z \cdot dz} \quad (1)$$

For the present Reynolds number Re=33,000, the swirl number S was calculated to be $S \approx 0.71$, consistent with the presence of a strong recirculation zone at the burner outlet.

3 Measurement Techniques

A main aim of these investigations is to characterize the flow instabilities occurring in swirling flows when forcing is applied to the flow. As instabilities could be also evidenced in the unforced case, it is appropriate to characterize the flow following the triple decomposition technique [20], where turbulent fluctuations u_{fluc} are split into a coherent part $\tilde{u}$ and a random part u'. Both parts are then added to the time-averaged velocity $\bar{u}$ to build the instantaneous velocity u

$$u = \bar{u} + u_{\text{fluc}} \quad (2)$$

$$u_{\text{fluc}} = \tilde{u} + u' \quad (3)$$

Thus, phase triggered PIV and phase-averaged velocities of the 2D LDA were used to capture the evolution of coherent structures characterized by $\tilde{u}$ in the unforced and forced cases. Both measurement techniques used the signal of the hydrophone (h) as a trigger signal to allow for the reconstruction of the triple decomposition. To reduce noise and avoid filter phase shifting, this signal was bandpass filtered with a single cutoff frequency corresponding to the dominant frequency observed.

3.1 PIV Measurement. PIV measurements were performed at the burner outlet in the (x_b, z_b)-plane. For this a standard PIV installation was used (Nd:YAG laser, 20 mJ per pulse, associated with a PCO Sensicam, 1024×1024 pixels, two image pairs per second). Seeding of water was achieved with 5 μm spherical silver coated particles. Data were processed in 32×32 pixel interrogation areas with 50% overlap. Interrogation areas were cross-correlated and a local median filter was used to eliminate spurious vectors. The eliminated data were replaced via interpolation from adjacent interrogation areas. The resulting vector field was used for an adaptive cross-correlation of the data, spurious data were filtered again and adaptive cross-correlation in 16×16 pixel interrogation areas was reapplied. The percentage of spurious vectors never exceeded 2% for any measurement plane.

The mean velocity profiles were computed with 500 image-pairs taken randomly. For the phase triggered acquisitions 60 image-pairs per phase were taken and averaged. This number was found to be high enough to capture the flow structure of interest but was not sufficient to obtain reliable statistical values of the flow as suggested by Wernert and Favier [21].

3.2 LDA Measurements. 2D LDA measurements were made using a Dantec two component system (Model No. 5500A-00 with BSA F60). The "sample and hold" acquisition of the bursts was set (2 ms dead time between two valid bursts, i.e., maximal data rate of 500 Hz), and the two velocity measurements were noncoincident. Data rates ranging from 100 Hz up to 500 Hz were achieved, depending on the location of the measurement probe. These values were sufficient to obtain a good resolution of the dominant frequencies of interest ranging below 10 Hz. The positioning of the LDA optic was ensured by a traversing system and positioning correction due to the different refraction indices (air,

glass, and water) was applied.

LDA measurements were mainly used to investigate the flow in the inlet slots. Measurements were performed at five axial positions from $x/D=-7/5D$ to $-3/5D$ in steps of $1/5D$ (Fig. 2(a)). Due to the complex geometry of the slot, which cannot be considered as a translated 2D profile with an increasing axial position x, a positioning procedure was defined. The burner angle was first set to $\theta=-20$ deg to ensure optical access into the inlet slot. The outer edge of the slot was used to position the measurement volume (point P in Fig. 2(b)). Then a translation along y_r and z_r (1 mm and 4 mm) positioned the measurement probe in the flow. The same procedure was repeated to define the points A to F shown in Fig. 2(a).

3.3 LDA Phase Averaging Processing. The velocity samples acquired by the LDA were first phase sorted in reference to the filtered reference signal, with a phase resolution of 1 deg (resulting in 360 bins). About 15,000 valid samples for each measurement point were taken. As the number of samples per bin did not allow for reliable statistical results, an estimate of the mean phase-averaged profile was obtained by fitting a Fourier series to the bin averaged profile, as described by Sonnenberger et al. [22]. Five harmonics were used and ensured a higher stability of the obtained profile against outliers resulting from the measurement. The formulation of the Fourier estimation of the mean velocity $u_{F,t}$ (here for the azimuthal velocity) was therefore

$$u_{F,t}(\phi) = \bar{u}_t + \sum_{m=1}^{5} a_m \cos(2\pi m f_0 \phi) + b_m \sin(2\pi m f_0 \phi) \quad (4)$$

where $\bar{u}_t$ is the mean velocity at the considered point, f_0 is the dominant frequency, and a_m and b_m are the Fourier coefficients of the harmonic m. To allow for a direct comparison of the amplitude and phase shift relationship between measurement points and hydrophone signal, the expression (4) was reformulated as follows:

$$u_{F,t}(\phi) = \bar{u}_t + \sum_{m=1}^{5} |\tilde{u}_{t,m}| \cos(2\pi m f_0 \phi + \angle (\tilde{u}_{t,m})) \quad (5)$$

with

$$\tilde{u}_{t,m} = a_m - i b_m \quad (6)$$

With this definition, the amplitude $|\tilde{u}_{t,m}|$ and the phase $\angle (\tilde{u}_{t,m})$ of the harmonic m are directly obtained. The same processing was also applied to the hydrophone signal as data of the hydrophone were sampled with a valid burst of the streamwise velocity and not continuously sampled. Figure 3 illustrates the effectiveness of the Fourier estimation in comparison to the bin averaging method. Measurements were performed at the position G at the burner outlet for the unforced flow (see position in Fig. 2). The left figure shows the phase sorted samples of the u_t component and the resulting bin averaging. It illustrates the strength of the random component u_t' in comparison to the coherent motion $\tilde{u}_t$. The Fourier estimation on the right figure smoothes the profile and allows for obtaining a better estimate of $\tilde{u}_t$.

In Fig. 3, it is also noticeable that the phase-averaged signal at the burner outlet is not sinusoidal but reproduces qualitatively the signal obtained in other experimental configurations [6].

The Fourier estimation was then used to calculate the phase shift between the first harmonic of the phase-averaged velocity at a chosen point i and the first harmonic of the signal of the hydrophone located above slot 1, which was calculated as follows:

$$\angle \varphi = \angle \tilde{u}_{t,1,i} - \angle \tilde{h}_1 \quad (7)$$

3.4 Definition of the Forcing Amplitude. The amplitude of the excitation showed a nonlinear response to the frequency and the different settings of the water test rig, such as the valve position. No global actuation amplitude could be satisfyingly defined
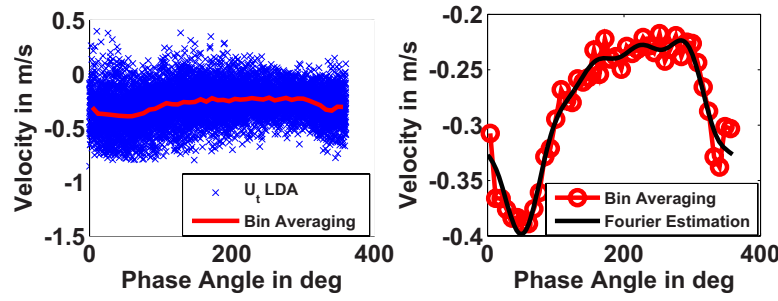
Fig. 3 Scatter plot of the phase-sorted azimuthal velocity u_t, bin averaging of the velocity (left) and comparison of the bin averaging with the Fourier estimation of the bin averaged velocity (right), $u_{F,t}$ for the unforced flow

from these settings, as resonance phenomena of the hydraulic pump with the piping system also occurred. Thus a local definition F_a of the forcing amplitude was chosen. It was constructed using the ratio of the first harmonic amplitude of the azimuthal velocity to its mean value at the arbitrarily chosen position C ($x/D=1$) in the slot S1

$$F_a = \left(\frac{|\tilde{u}_{t,1}|}{\bar{u}_t} \right)_C \qquad (8)$$

With this definition, forcing amplitudes of up to $\pm 90\%$ for selected frequencies were achievable. The corresponding forcing Strouhal number St_f was based on the forcing frequency f, the burner outlet diameter D, and the mean bulk streamwise velocity U_0 based on this diameter.

3.5 Proper Orthogonal Decomposition. A low-dimensional characterization of the fluctuating velocity field is obtained by proper orthogonal decomposition. POD decomposes the flow in spatial dependent modes and time-dependent mode coefficients. The POD modes are sometimes referred to as coherent structures of the flow field. The decomposition represents the flow field in an optimally compact fashion in the sense that $\|\mathbf{u}_{\text{fluc}}(\mathbf{x},t) - \Sigma_{j=1}^{N} a_j(t)\mathbf{u}_j(\mathbf{x})\|^2$ is minimal for any N over the class of all orthonormal bases. The fluctuating velocity field is decomposed as follows:

$$\mathbf{u}_{\text{fluc}}(\mathbf{x},t) \approx \mathbf{u}_{\text{fluc}}^{(N)}(\mathbf{x},t) = \sum_{j=1}^{N} a_j(t)\mathbf{u}_j(\mathbf{x}) \qquad (9)$$

where N is the number of modes, $\mathbf{u}_j$ are the POD modes, and the mode coefficients are labeled a_j.

The optimality condition leads to the following eigenproblem:

$$\int_{\Omega} \overline{\mathbf{u}_{\text{fluc}}(\mathbf{x}) \otimes \mathbf{u}_{\text{fluc}}(\mathbf{x}')}\mathbf{u}_j(\mathbf{x}')d\mathbf{x}' = \lambda_j \mathbf{u}_j(\mathbf{x}) \qquad (10)$$

where Ω is the considered flow domain. The λ_j are the eigenvalues corresponding to the eigenfunctions $\mathbf{u}_j$, which are called POD modes. $\overline{\mathbf{u}_{\text{fluc}}(\mathbf{x}) \otimes \mathbf{u}_{\text{fluc}}(\mathbf{x}')}$ is the two-point space-time correlation tensor ($\otimes$ is the dyadic product). The eigenvalues λ_j represent the contribution of the mode j to the mean turbulent kinetic energy (TKE). The modes are ordered by decreasing energy contribution (optimality condition). The time coefficients can be obtained by taking the inner product with the corresponding mode

$$a_j(t) = \int_{\Omega} \mathbf{u}_{\text{fluc}}(\mathbf{x},t)\mathbf{u}_j(\mathbf{x})d\mathbf{x} \qquad (11)$$

A full discussion of the POD framework may be found in Holmes et al. [23].

4 Unforced Flow of the Burner

4.1 Natural Coherent Structure Visualization. The first step of the investigation is to characterize the unforced flow field, as well as the dominant structures and their characteristic frequencies. Figure 4 shows the PIV results of the mean unforced flow ($St_f=0$) at the burner outlet in the (x_b,z_b)-plane. The contour plot of the streamwise velocity u_x on which the vector plot (u_x,u_r) is superposed, shows a central recirculation zone surrounded by a conical jet, which is typical for this kind of swirling flow. The signal of the hydrophone showed a dominant frequency corresponding to $St_n \approx 0.92$. This frequency could also be observed in the u_x and u_t components of the LDA in the shear layer, as shown by the power spectrum densities (PSD) of their fluctuating parts, $\tilde{u}_{x,\text{fluc}}$ and $\tilde{u}_{t,\text{fluc}}$, in Fig. 5. Further measurement showed that the dimensionless frequency St_n of the helical structure was also independent of the Reynolds number, confirming that this instability
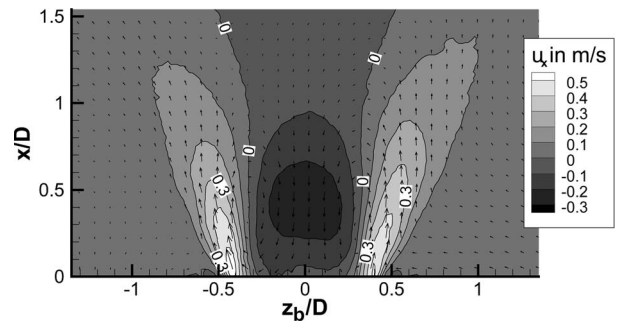

Fig. 4 Contour plot of the mean streamwise velocity $\bar{u}_x$ in m/s with the vector plot of the velocity in the (x_b,z_b)-plane, unforced flow
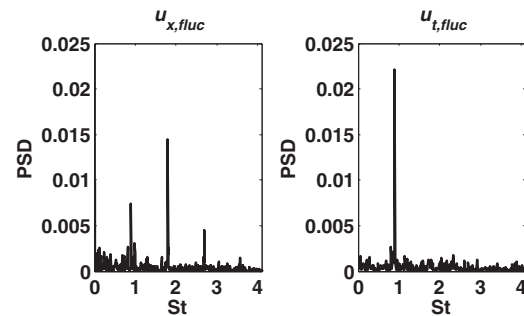

Fig. 5 Frequency spectra of the $u_{x,\text{fluc}}$ (left) and $u_{t,\text{fluc}}$ (right) components for the unforced flow, in the shear layer at the burner outlet (G position, $x=D/4$, $y=0$, and $z=-50$ mm)
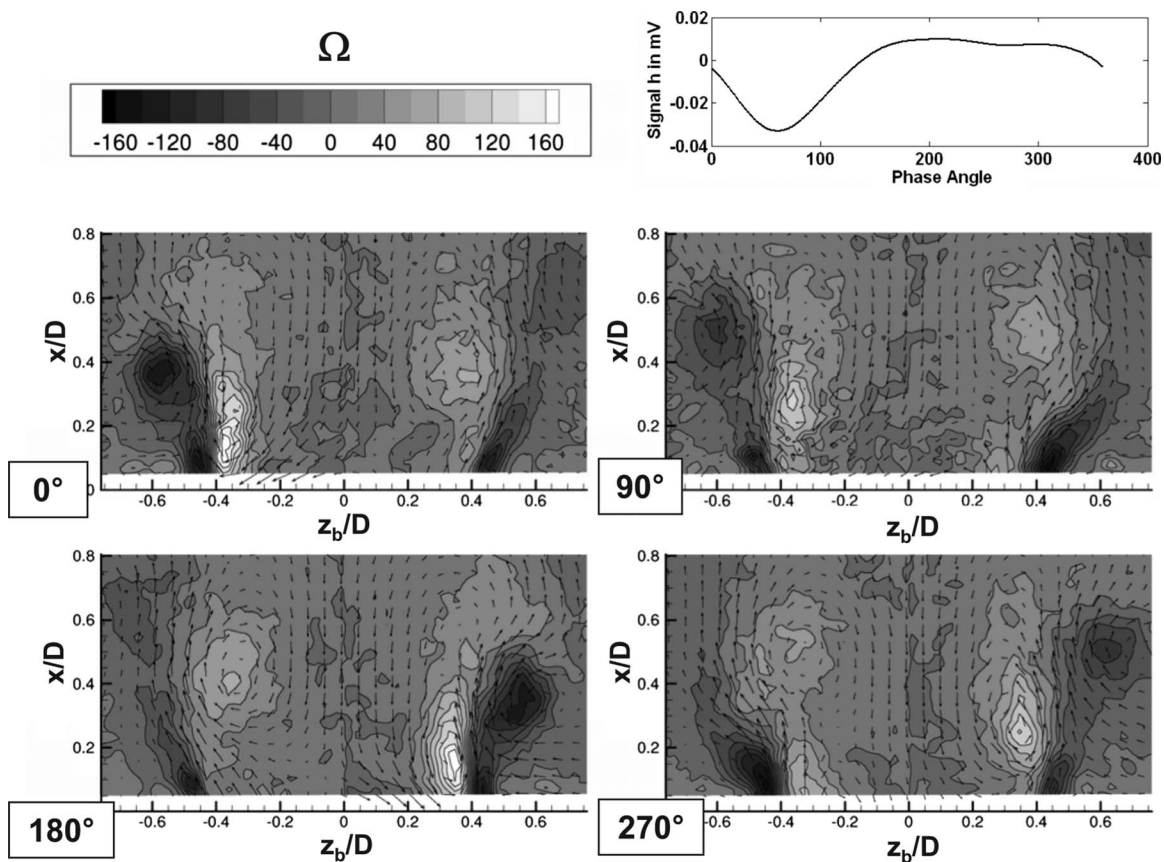
Fig. 6 Phase-averaged color maps of the azimuthal vorticity Ω (in s^{-1}) in the (x_b, z_b)-plane of the unforced flow, which evidences the natural helical mode. Four phases of the hydrophone signal (top right) were used to trigger the acquisition. The arrows represent the velocity vectors.

is related to a flow instability.

To visualize this flow structure, phase triggered PIV measurements were performed as described in Sec. 3. The azimuthal vorticity Ω defined as

$$\Omega = \frac{\partial u_x}{\partial r} - \frac{\partial u_r}{\partial x} \qquad (12)$$

was used to plot the data, with r corresponding to the distance of a considered point to the centerline of the flow. This definition characterizes more easily rotational systems, as a rotational structure centered on $r/D=0$ will have the same vorticity sign (and hence the same color in the color maps) in the positive ($z_b/D \geq 0$) or negative ($z_b/D \leq 0$) axial half planes. Four of the eight phase angles acquired, which are presented in Fig. 6, clearly show the streamwise evolution of one helical structure. The phase angle 0 deg appears indeed to be the axial symmetric picture of the phase angle 180 deg. This helical structure is made up of two counter rotating vortices, which evolve downstream as the phase angle increases.

As the helical structure could be detected at the burner outlet, the question of what happen to the slot needs to be answered. To this end, LDA measurements were performed in slot 1 at the previously defined axial positions. Then, the complete system hydrophone/burner was rotated by 180 deg allowing for an access to the second slot.

The power spectrum densities presented in Fig. 7 clearly show that an oscillation at the same frequency (St ≈ 0.92) is also present upstream within the slots. This oscillation can be found back near the burner apex (position E). Furthermore, the relative amplitude of the oscillation in both slots for the azimuthal velocity $\tilde{u}_t$ is plotted along the axial position. The amplitude of the fundamental

frequency is calculated following Eq. (8), this time applied at the considered point. This amplitude increases as a power 4 of the axial position, but remains still lower than the amplitude observed in the shear layer at position G.

The evolution of the phase shift between the azimuthal velocities in the two slots and the hydrophone is shown in Fig. 8. A phase shift of about 180 deg is visible, confirming the helical nature of the oscillations in the burner slots. This plot facilitates an estimation of the axial wavelength λ of the instability into the burner, which is $\lambda = 2.25D$.

This wavelength decreases strongly to $\lambda \approx 0.5D$ at the burner outlet, as can be seen in Fig. 6, where a half wavelength of 0.25D can be estimated at each phase angle presented. This decrease is mainly due to the change in the flow field induced by the geometry of the dump section.

4.2 Determination of the Mode Sign and Phase Equation. As the PIV phase locked measurement showed that the structure is traveling downstream, only the sense of rotation (i.e., clockwise or counterclockwise rotation) determined at one axial position is necessary to fully characterize the structure (see Ref. [8] or Ref. [24] for more details). The determination of the sign of the helical mode was performed by introducing a second hydrophone probe. One hydrophone (h_2) was fixed over slot 1, while the angle β of the other hydrophone (h_1) was varied on the circumference of the burner (see sketch in Fig. 9). The cross-correlation R_{h1h2} of both signals gives then the resulting time lag and hence phase lag $\angle h_1 h_2$ depending on the angle β. Figure 9 shows that both angles have the same sign and, regarding the common definition of R_{h1h2}, this means that the signal h_1 precedes the signal h_2 when $\beta \in [0, 180]$ and follows h_2 when $\beta \in [-180, 0]$. The helix is thus wind-
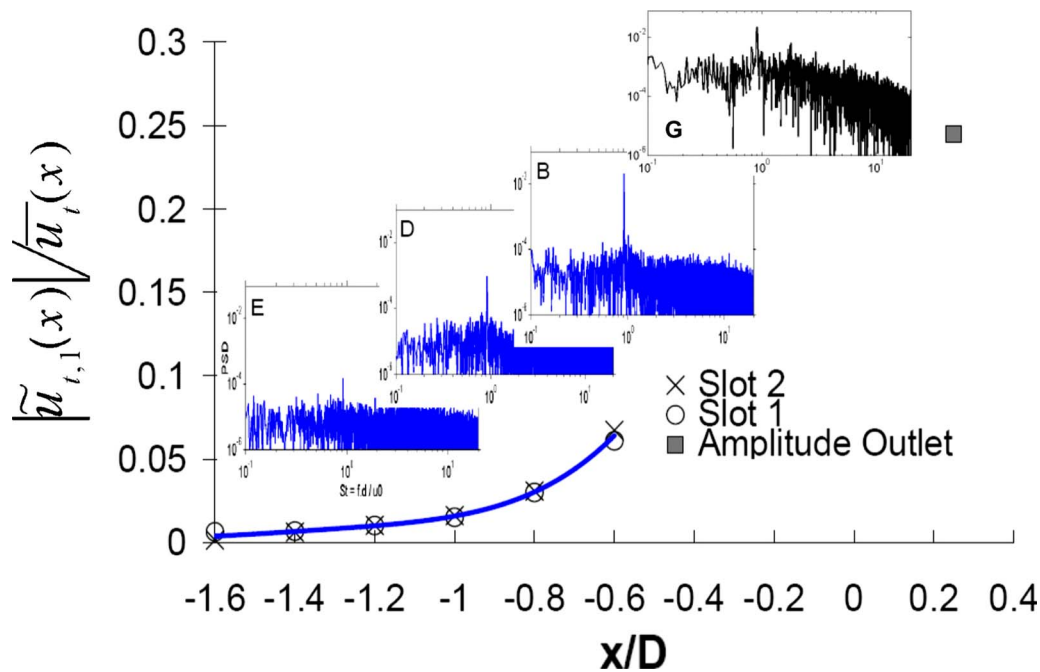
Fig. 7 Relative oscillation amplitude of the natural frequency for u_t over the axial position for the unforced flow. Spectrum of the signal at the different locations (E, D, B, and shear layer G) is shown. A best fit power four polynomial is applied to the data.

ing in the same sense as the swirling motion, and the mode sign is positive ($m=1$), confirming the results of the LES simulation on the same burner model presented by Duwig et al. [10].

Fig. 8 Phase relationship between the tangential velocity $\tilde{u}_t$ and the hydrophone signal h within Slots 1 and 2 of the burner depending on the axial position x/D for the unforced flow

Fig. 9 Phase angle $\angle h_1 h_2$ of the hydrophone signals as a function of the angle β

With the data acquired, as discussed above, it is possible to reconstruct the phase relation φ_{hel} of the helical wave into the burner.

$$\varphi_{hel}(x,\theta,t) = (kx + m\theta - \omega t) \qquad (13)$$

with the measured parameter, $k=2\pi/(2.25D)$, $m=1$, and $\omega=2\pi\,St_n\,U_0/D$. This relation may be taken from Ref. [8] or Ref. [24] and is valid for a flow rotating counterclockwise when viewed from the downstream x-direction, as is the case here.
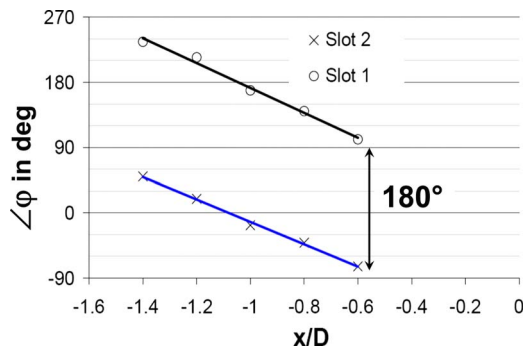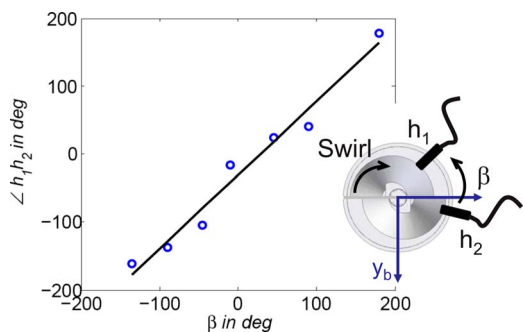
4.3 Transposition of the Water Experiment to Gaseous Experiment. To verify that the results of the water test rig could be transposed to real gas flow conditions, similar tests were conducted on a similar burner in an air test rig [25]. A dominant frequency corresponding to the same Strouhal number $St=0.92$ was measured in the inlet slot, confirming that the water laboratory experiments catch the same dominant flow phenomena as in the gaseous case.

4.4 Explanation of the Origins of Flow Oscillations in the Slot. The previous results demonstrate that the helical instability, which was observed at the burner outlet, is also present upstream of the inlet slot. In order to explain the phenomena observed, information on the flow field inside the burner was needed. Some of the required information was obtained from a steady computational fluid dynamics (CFD) simulation of the flow field performed by the authors but, as yet, is still unpublished. The domain extending between $x/D=-2.8$ and $x/D=4$ was calculated using a first order Reynolds average Navier–Stokes (RANS) solver in CFX 10.0. A k-ε turbulence model was employed together with an unstructured mesh that was refined in regions containing large velocity gradients. They showed that the vortex breakdown (VBD) already occurs in the burner and the stagnation point of the recirculation zone narrows the apex of the burner. In other words, the recirculation zone is already present in the burner. As the helical instability is closely related to the VBD phenomenon, the steady numerical simulation confirms also the experimental observation
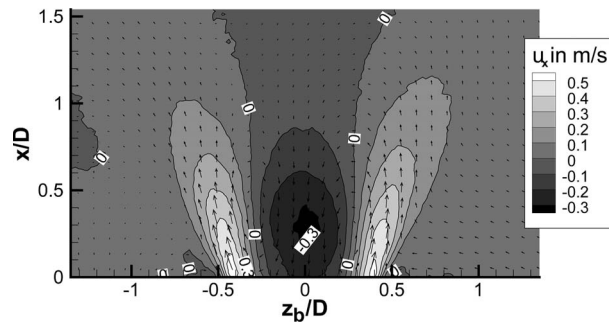
Fig. 10 Contour plot of the mean streamwise velocity $\overline{u}_x$ in m/s with the vector plot of the velocity in the (x_b, z_b)-plane, forced flow at $St_f \approx 0.92$

of Sec. 4.1.

The first explanation of the velocity oscillations at the burner inlet presupposes that the helical structure is directly responsible for pressure and velocity oscillations at the inlet. This helical structure may be seen by the slots as a rotating pressure field, which changes periodically the local pressure loss coefficient over the slot length. As the overall pressure drop over the burner remains constant, this is also the case of the pressure drop along a streamline of the mean flow. An increase in the local pressure drop coefficient will thus lead to a reduction in the velocity to keep the mean total pressure constant. Thus, the velocity oscillations will also follow the periodic motion of the helical instability.

Another explanation deals directly with the nature of the flow. The VBD is related to a change in the flow nature and can be explained by a transition from a supercritical state to a subcritical one [13]. The subcritical nature of the flow is a necessary condition to obtain an absolute instability, which allows for the pressure field oscillation associated with the coherent structures to propagate upstream of the perturbation or VBD location. These pressure oscillations would also lead to velocity oscillations. As the VBD already occurs in the burner, there is no chance for the flow to be supercritical in the burner, as suggested by Keller et al. [26], which is a necessary condition to avoid oscillations in the slots.

These results are important for the understanding of the mixing process fuel/air of the burner as the injection of fuel is performed in the slots. In fact, Flohr et al. [27] underlined that the turbulent scalar transport induced by coherent motion may have a dominant contribution to the global turbulent transport for the same burner. The natural velocity oscillations evidenced here will lead to fuel/air ratio oscillations, which may excite unstable modes of the combustor.

5 Impact of Axial Forcing on the Flow Field

5.1 Forcing at the Natural Frequency ($St_f \approx 0.92$). First, the flow was excited at the natural frequency previously measured ($St_f \approx 0.92$), and the same measurements as in the unexcited case were performed. The amplitude F_a of forcing was set to 50%. Figure 10 shows the resulting flow field at the burner outlet. Compared with the unforced case presented in Fig. 4, it clearly shows that the forcing has a negligible impact on the mean velocity field at the burner outlet. This is confirmed by the radial profiles of the axial and radial velocities presented in Fig. 11, which show little changes between the two cases. The inner recirculation zone slightly decreases when forcing is applied and the axial velocity on the centerline near the burner outlet also decreases. Beside those minor changes, the mean flow field remains mostly unchanged. It is not the case of the coherent motion which shows completely different patterns with forcing at the natural flow frequency as shown by the phase-averaged vorticity plots in Fig. 12. For this forcing frequency, the helical structure is replaced by an axially symmetric vortex ring.

As for the unforced flow, the phase relationship between velocity in the slot and the hydrophone was recorded for three forcing amplitudes F_a and is presented in Fig. 13. The forcing completely eliminates the phase shift existing between the different axial positions in the unforced configuration as the phase angle $\angle \varphi$ remains constant. The phase shift of 60 deg obtained for the three forcing amplitudes is due to a phase shift between the hydrophone and velocity, as pressure oscillations coming from the excitation are not in phase with the velocity oscillation in the shear layer.

The observation of the oscillation amplitude along the slot for the three forcing amplitudes is shown in Fig. 14. An increase in the axial position leads also to a slight increase in the oscillation amplitude in the slot. This observation may be of interest regarding the control of combustion by fuel injection. On one hand, one would prefer a steady fuel injection at the bottom of the burner, where flow oscillations and hence fuel mixing oscillations are lower than near the burner outlet. On the other hand, an unsteady
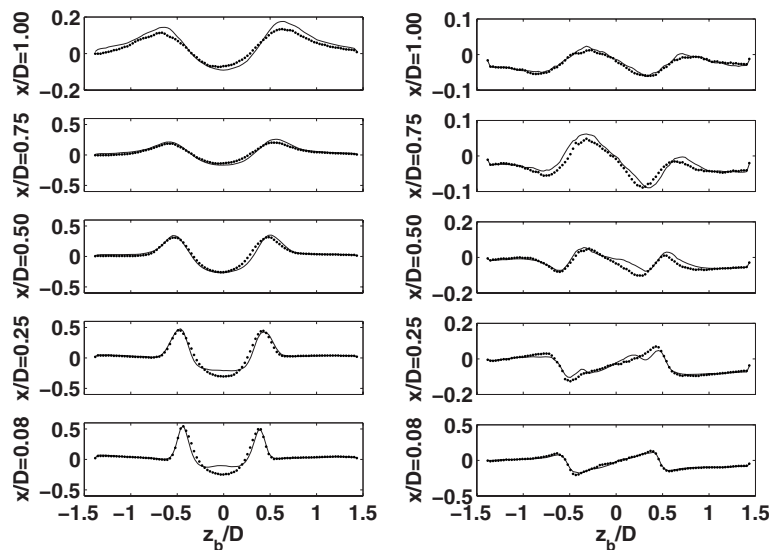

Fig. 11 Line plot of the mean streamwise velocity $\overline{u}_x$ (left) and radial velocity $\overline{u}_r$ (right), in m/s, for the unforced ($St_f=0$, –) and forced ($St_f \approx 0.92$, ●) cases
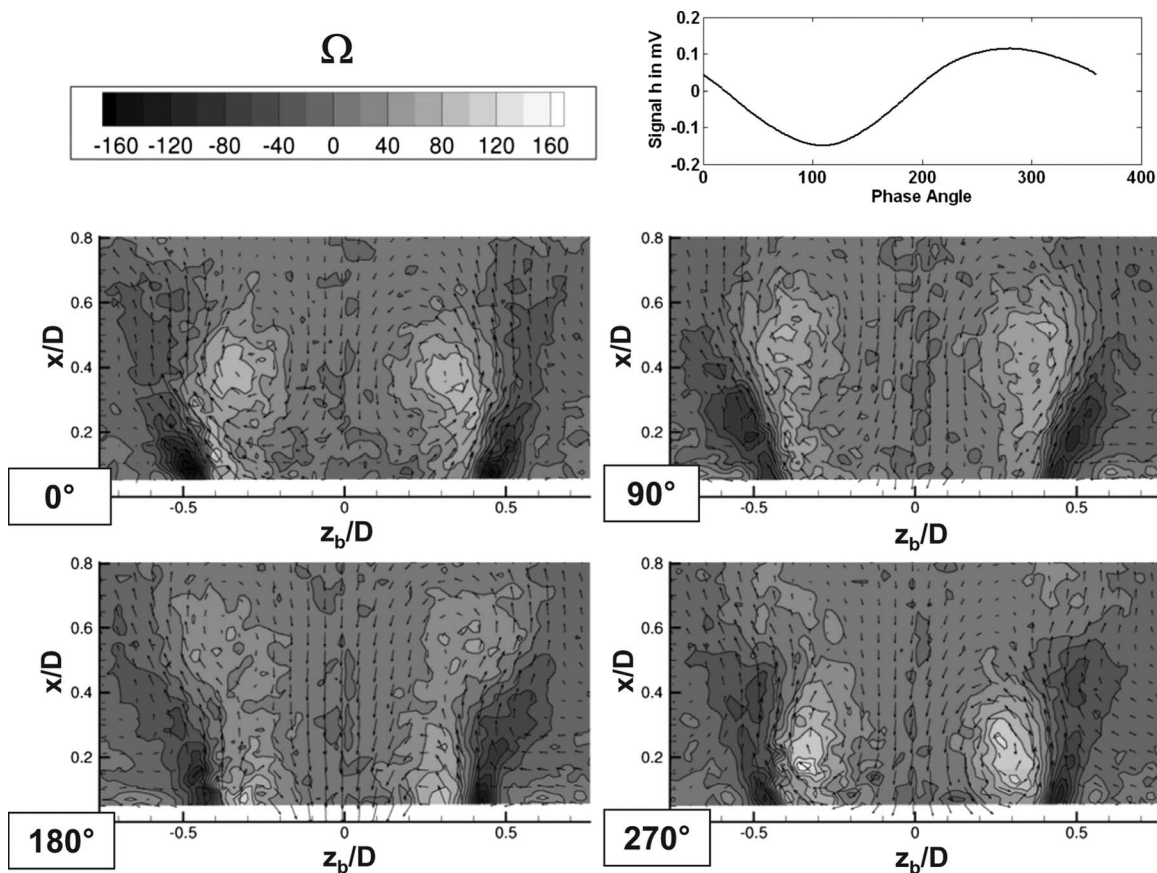
Fig. 12 Phase-averaged azimuthal vorticity Ω (in s^{-1}) in the (x_b, z_b)-plane of the forced flow at $St_f \approx 0.92$, which shows the axisymmetric structure. Four phases of the hydrophone signal (top right) were used to trigger the acquisition. The arrows represent the velocity vectors.

injection of fuel at the frequency of the instability (active control) may be more effective near the burner outlet if the phase between the fuel injection and the main flow is properly adjusted.

Furthermore, except for the extremely strong forcing amplitude ($F_a = 90\%$) where back flow occurs, the profiles of the mean velocity (Fig. 15) and oscillation amplitude appear similar from the apex of the burner to $x/D \approx -0.8$. Mean radial profiles across the slots of the axial and tangential velocities showed also the same results. Thus, except for a deviation in the profiles at $x/D > -0.8$ and $F_a > 50\%$, the mean distribution of the flow in the burner inlet slots is only slightly influenced by the forcing.

5.2 Forcing at a Frequency Not Related to the Natural Flow Frequency($St_f \approx 1.3$). The impact of an excitation, which did not correspond to any harmonic of the unforced flow was
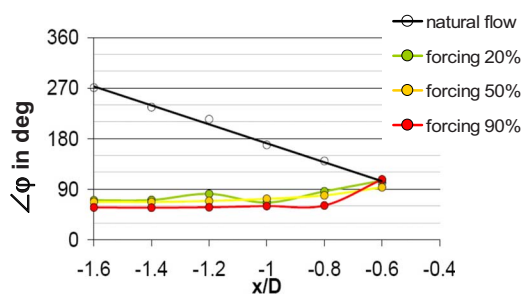
investigated. For this, the PSD spectra of the LDA measurements in the slot ($x/D = -4/5D$, point B) and in the shear layer (x
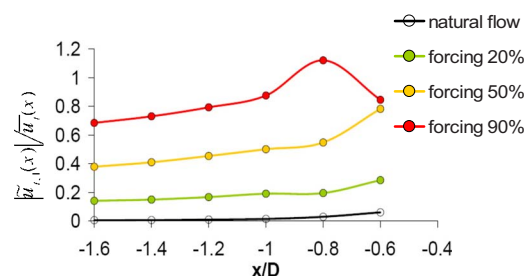

Fig. 14 Relative oscillation amplitude of $\tilde{u}_t$ depending on the axial position x/D for three forcing amplitudes at $St_f \approx 0.92$

Fig. 13 Phase relationship between the tangential velocity $\tilde{u}_t$ and the hydrophone signal h within slot 1, for three forcing amplitudes at $St_f \approx 0.92$
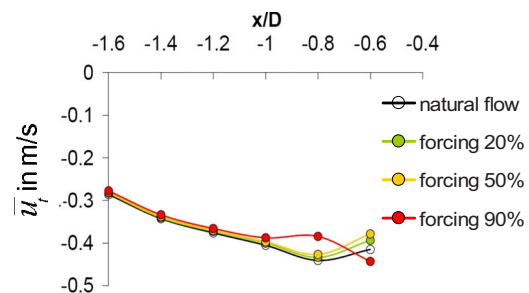

Fig. 15 Impact of the excitation on the mean flow velocity $\bar{u}_t$ in slot 1 at $St_f \approx 0.92$
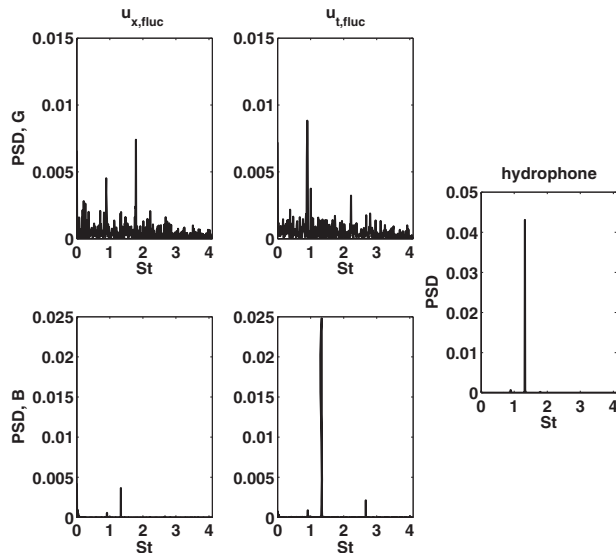
Fig. 16 Spectra of $u_{x,\text{fluc}}$ and $u_{t,\text{fluc}}$ in the shear layer (**G**) and in Slot (**B**) for $\text{St}_f \approx 1.3$ and $F_a = 10\%$. The spectrum of the hydrophone is shown in the right plot.

Fig. 17 Repartition of the turbulent kinetic energy within the POD modes for the three with PIV investigated cases

$= D/4$, $y = 0$, $z = -50$ mm, point G) were compared. The results for the streamwise and azimuthal turbulent velocities at $\text{St}_f \approx 1.3$ are presented in Fig. 16. They show that the dominant frequency in the shear layer is equal to $\text{St} \approx 0.9$ even if the forcing is applied at a higher frequency.

The jet is thus not receptive to this forcing frequency, and no lock-in of the vortex shedding can be achieved at the burner outlet. These results show the same trends as those of Khalil et al. [17], with the difference that the lock-in of the vortex shedding occurred in their study at frequencies of up to $\text{St}_f = 2 \, \text{St}_n$. As their experimental setup is totally different, one cannot expect the same results to be obtained in the present case. Thus the lock-in phenomenon, if present, may occur over a narrower frequency bandwidth.

With the measurement setup used, the phase-averaged PIV measurement did not reveal any flow structure when forcing was applied at higher frequencies than the natural instability frequency. The signal of the hydrophone recorded mainly the pressure oscillations induced by the forcing at $\text{St} \approx 1.3$ and was not appropriate to be used as a trigger signal at $\text{St} \approx 0.9$ for the phase-averaged PIV (see Fig. 16). POD analysis of the PIV snapshots was thus performed to obtain the missing information, particularly when forcing is applied at higher frequencies than the natural one.

6 Analysis of Flow Structures With POD

6.1 Turbulent Kinetic Energy Distribution. The POD analysis of the velocity vector field (u_x, u_r) was performed for the three cases: $\text{St}_f = 0$, $\text{St}_f \approx 0.92$, and $\text{St}_f \approx 1.55$. In all cases, at least 200 modes were necessary to resolve 90% of the turbulent kinetic energy, which confirms the complexity of the unforced as well as the forced flows. However, the first POD modes still represent a significant fraction of the TKE, as shown in Fig. 17. Regarding the unforced flow, the first five modes resolve 25% of the TKE, i.e., important flow features are captured with a relatively small number of modes. The normalized modal TKE of the first mode matches also well with the POD results from the numerical simulation of Duwig et al. [10] (6.2% compared with 5.7%).

As we compare the TKE distribution of the three flow cases presented in Fig. 17, it is apparent that the natural flow and the flow forced at $\text{St}_f \approx 1.55$ are similar, except for the differences in the second mode. Actuation with the natural flow frequency ($\text{St}_f \approx 0.92$) presents a more significant change in the energy reparti-
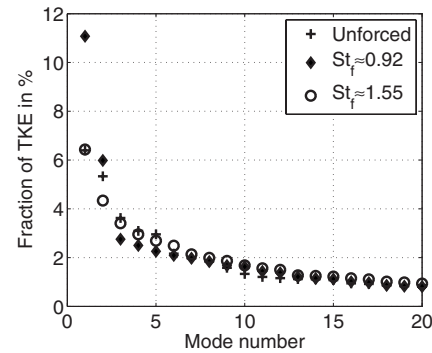
tion, as the first mode contains twice as much energy as the first mode of the unforced flow. Hence this explains partly why the $\text{St}_f \approx 0.92$ case will show a stronger change in the structures than the $\text{St}_f \approx 1.55$ case when compared with the unforced flow.

6.2 Mode Shape. The resulting modes of the above mentioned POD method are defined in the velocity (u_x, u_r). As the mode structures are of interest, the modes are rewritten in the azimuthal vorticity $\Omega(\mathbf{x})$, which is shown in Fig. 18. For each case (from left to right), the mean flow and the first four POD modes are presented (from top to bottom). Antisymmetric structures can be observed for the unforced and the forced case $\text{St}_f \approx 1.55$ (modes 1–3), whereas the forced case corresponding to $\text{St}_f \approx 0.92$ shows axisymmetric structures. A helical mode can be associated with the antisymmetric structures, which confirms that a helical structure is present at the burner outlet for the case $\text{St}_f \approx 1.55$. The main difference between both helical structures is that the helix of the unforced flow is more stretched in the $\mathbf{x}$ and $\mathbf{r}$ directions than for the $\text{St}_f \approx 1.55$ case. For the latter, almost one revolution period of the helix is visible, and the axial wavelength is smaller. The radial stretching is due to the jet opening angle, which is lower for the forced case. Forcing at $\text{St}_f \approx 1.55$ leads to a small jet opening angle and promotes a lower axial decay of the coherent structures.

POD modes 2 and 3 of the $\text{St}_f \approx 0.92$ case form a pair, exhibiting strong similarities and a phase shift with respect to each other in the axial direction. They indicate two counter-rotating vortices at $|r/D| \approx 0.5$ and an axial displacement of the structure. Since the snapshots are not correlated in time, it is not possible to track with the POD analysis the evolvement of this structure. The first mode of this case describes a mean flow correction of the velocity flow field, which may correspond to a slow variation in the central recirculation zone. A similar analysis can be done with the first two POD modes of the case $\text{St}_f \approx 1.55$ or modes 1 and 3 of the unforced flow.

The fourth mode of case $\text{St}_f \approx 1.55$ is axially symmetric, showing that a low energy axial symmetric structure is present at the burner outlet. On the contrary, mode 4 of case $\text{St}_f \approx 0.92$, exhibits an antisymmetric structure, while the three first modes are symmetric. Thus, the forcing does not necessarily suppress some structures, but redistributes the modal contribution on the TKE.

6.3 Sensitivity Analysis. A sensitivity analysis was performed in order to see how many snapshots are needed for a good representation of the dominant coherent structures. Therefore, the POD framework was applied on $M = 63$, 125, 250, and 500 snapshots. The unforced flow was chosen for this analysis and modes 1, 3, 7, and 9 are presented in Fig. 19. As expected, an increase in the number of snapshots smoothes the shape of the POD modes. Especially, for modes 1–7, the shape of the modes obtained with 500 snapshots is already recognizable in the modes obtained with four times less snapshots. Mode 9 shows also strong similarities in
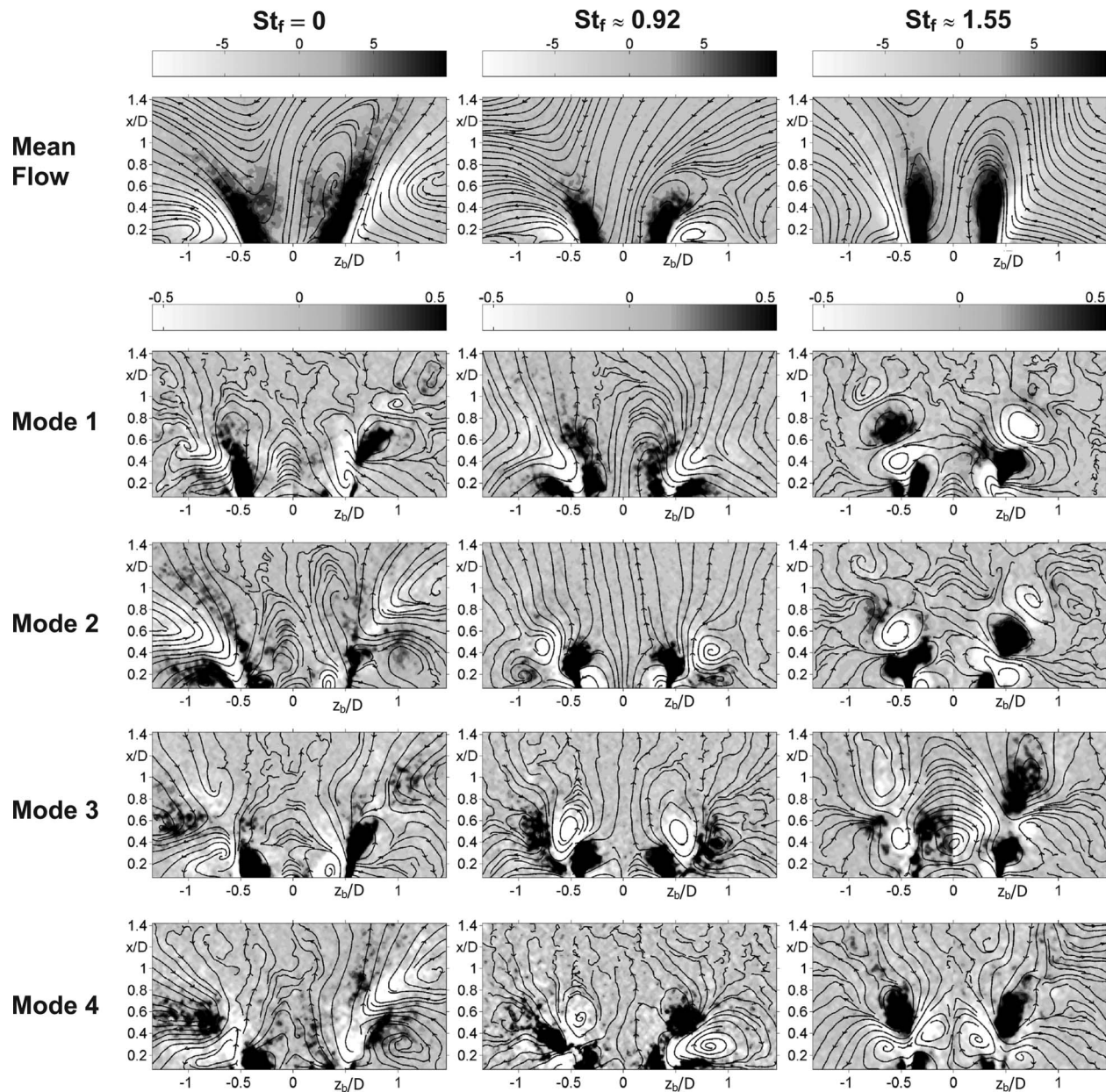
Fig. 18 Contour plot of the azimuthal vorticity Ω resulting from the POD analysis of the snapshots in the (x_b, z_b)-plane. The mean vorticity and the first four (1–4) dominant modes for all three investigated cases are presented and show the dominant coherent flow structures. The limits of the gray scale are set to emphasize the vorticity sign of the structures, as absolute vorticity values are not of interest. Superposed are streamline representations of the corresponding modes.

structures resulting from 500 and 250 snapshots. Thus, 500 snapshots are sufficient if one is only interested in the dominant flow structures.

7 Conclusion and Outlook

The impact of axial forcing on the flow field of a swirl burner was investigated and compared with its unforced counterpart. The impact of different oscillation frequencies and amplitudes on the flow at the inlet and outlet of the burner was documented.

The natural helical mode $(m=+1)$ typical for those types of flows could be captured by phase-averaged LDA and PIV at the burner outlet. The helical wave could be also found in the inlet slots of the burner, upstream of the stagnation point located in the burner. Thus the flow from the inlet of the burner is subject to an absolute instability, which needs to be taken into account for further modeling of the fuel/air mixing.

The forcing frequencies and amplitudes had little impact on the mean velocity field at the burner inlet and outlet, but had a stronger influence on the coherent flow motion. Axisymmetrical forcing of the flow leads to a lock-in of the oscillation in the slot onto the forcing frequency. However, the response of the flow at the burner outlet is dependent on the forcing frequency as follows.

- Forcing at the natural frequency leads to a switch of the helical structure to an axisymmetric one.
- Forcing at a higher frequency than the natural frequency $(St_f \approx 1.3)$ shows no lock-in of the vortex shedding frequency onto the applied frequency. The POD analysis of PIV snapshots shows clearly that a helical structure is still present at the burner outlet even if the forcing applied is axially symmetric $(St \approx 1.55)$.
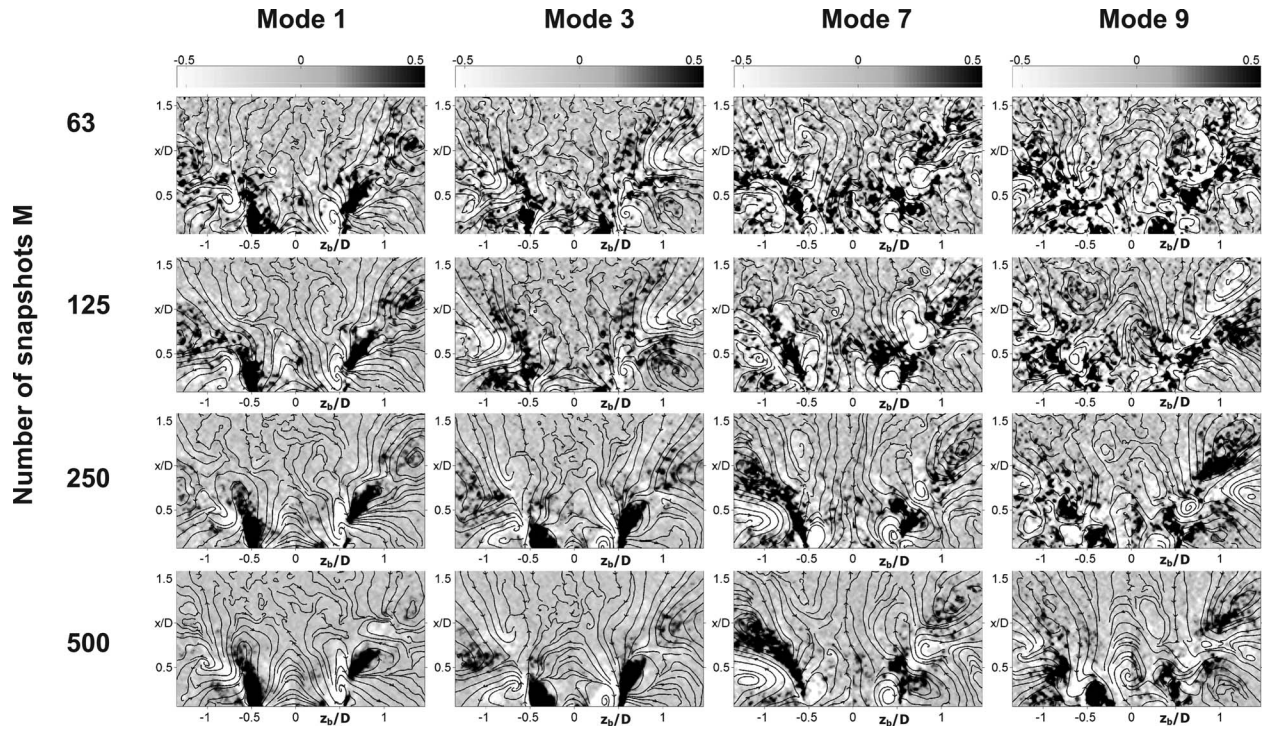
| | Mode 1 | Mode 3 | Mode 7 | Mode 9 |

Fig. 19 Sensitivity of the POD to the number *M* of PIV snapshots (63, 125, 250, and 500) taken for the analysis. Modes 1, 3, 7, and 9 of the unforced flow are presented.

The proper orthogonal decomposition performed on experimental data appears to be an appropriate tool to capture physical properties of the flow, which cannot be easily and directly measured by the present measurement configuration. Even if the flow is quite complex, as more than 200 modes were needed to resolve 90% of the total kinetic energy, the five dominant modes of the unforced and forced flows still represented 25% of the TKE. Low order modeling, based on the approach described in Ref. [28], may represent the physical mechanisms sufficiently for further work related to closed-loop control.

Acknowledgment

Nomenclature

$$
\begin{aligned}
a_j &= \text{mode coefficients from POD}\\
a_m &= \text{Fourier series coefficient}\\
b_m &= \text{Fourier series coefficient}\\
D &= \text{burner diameter}\\
f &= \text{excitation frequency}\\
F_a &= \text{forcing amplitude}\\
h &= \text{hydrophone signal}\\
r=\sqrt{(y^2+z^2)} &= \text{radius}\\
\mathbf{u}_j &= \text{POD modes}\\
u_x &= \text{streamwise velocity}\\
u_r &= \text{radial velocity}\\
u_t &= \text{azimuthal velocity}\\
U_0 &= \text{bulk velocity at the burner outlet}\\
x &= \text{streamwise axis}\\
(x_b, y_b, z_b) &= \text{coordinate system of the burner}\\
(x_r, y_r, z_r) &= \text{coordinate system of the test rig}\\
\mathbf{R}_{h1, h2} &= \text{cross-correlation function}
\end{aligned}
$$

$$
\begin{aligned}
\text{Re}=U_0 D/\nu &= \text{Reynolds number}\\
\text{St}=fD/U_0 &= \text{Strouhal number}\\
\text{St}_f=f_{\text{forcing}}D/U_0 &= \text{Strouhal number of the forcing}\\
\angle\varphi &= \text{phase angle between the hydrophone}\\
&\quad\text{and LDA signal}\\
\varphi_{\text{hel}} &= \text{phase function of the helical wave}\\
\lambda &= \text{axial wavelength}\\
\lambda_j &= \text{eigenvalues of the POD Analysis}\\
\nu &= \text{kinematic viscosity}\\
\omega &= \text{precessing frequency}\\
\Omega=\partial u_x/\partial r - \partial u_r/\partial x &= \text{azimuthal vorticity}\\
\overline{(\cdot)} &= \text{time-averaged quantity}\\
\widetilde{(\cdot)} &= \text{coherent part of the turbulent motion}\\
(\cdot)' &= \text{turbulent quantity}
\end{aligned}
$$

References

[1] Lieuwen, T., and Zinn, B. T., 1998, "The Role of Equivalence Ratio Oscillations in Driving Combustion Instabilities in Low NOx Gas Turbines," *Proceedings of the 27th Symposium (International) on Combustion*, Combustion Institute, Boulder, CO, Aug. 2–7, pp. 1809–1816.

[2] Bothien, M. R., Moeck, J. P., Lacarelle, A., and Paschereit, C. O., 2007, "Time Domain Modelling and Stability Analysis of Complex Thermoacoustic Systems," Proc. Inst. Mech. Eng., Part A, **221**(5), pp. 657–668.

[3] Paschereit, C. O., Gutmark, E. J., and Weisenstein, W., 1999, "Coherent Structures in Swirling Flows and Their Role in Acoustic Combustion Control," Phys. Fluids, **11**, pp. 2667–2678.

[4] Poinsot, T., Trouvé, A., Veyante, D., Candel, S., and Esposito, E., 1987, "Vortex Driven Acoustically Coupled Combustion Instabilities," J. Fluid Mech., **177**, pp. 265–292.

[5] Panda, J., and McLaughlin, D. K., 1994, "Experiments on the Instabilities of a Swirling Jet," Exp. Fluids, **6**, pp. 263–276.

[6] Syred, N., 2006, "A Review of Oscillation Mechanisms and the Role of the Precessing Vortex Core (PVC) in Swirl Combustion Systems," Prog. Energy Combust. Sci., **32**, pp. 93–161.

[7] Lucca-Negro, O., and O'Doherty, T., 2001, "Vortex Breakdown: A Review," Prog. Energy Combust. Sci., **27**, pp. 431–481.

[8] Fernandes, E. C., Heitor, M. V., and Shtork, S. I., 2006, "An Analysis of Unsteady Highly Turbulent Swirling Flow in a Model Vortex Combustor," Exp. Fluids, **40**, pp. 177–187.

[9] Wang, S., and Yang, V., 2005, "Unsteady Flow Evolution in Swirl Injectors With Radial Entry. II. External Excitations," Phys. Fluids, **17**, p. 045107.

[10] Duwig, C., Fuchs, L., Lacarelle, A., Beutke, M., and Paschereit, C. O., 2007, "Study of the Vortex Breakdown in a Conical Swirler Using LDV, LES and POD," ASME Paper No. GT2007-27006.

[11] Paschereit, C. O., and Gutmark, E. J., 2004, "The Effectiveness of Passive Combustion Control Methods," ASME Paper No. 2004-GT-53587.

[12] Rodriguez-Martinez, V. M., Dawson, J. R., Syred, N., and O'Doherty, T., 2003, "The Effect of Expansion Plane Geometry on Fluid Dynamics Under Combustion Instability in a Swirl Combustor," AIAA Paper No. 2003-116.

[13] Escudier, M. P., and Keller, J. J., 1985, "Recirculation in Swirling Flow: A Manifestation of Vortex Breakdown," AIAA J., **23**, pp. 111–116.

[14] Paschereit, C. O., Oster, D., Long, T. A., Fiedler, H. E., and Wygnanski, I., 1992, "Flow Visualization of Interactions Among Large Coherent Structures in an Axisymmetric Jet," Exp. Fluids, **12**, pp. 189–199.

[15] Suzuki, H., Kasagi, N., and Suzuki, Y., 2004, "Active Control of an Axisymmetric Jet With Distributed Electromagnetic Flap Actuators," Exp. Fluids, **36**, pp. 498–509.

[16] Lacarelle, A., Moeck, J. P., Konle, H. J., Vey, S., Nayeri, C. N., and Paschereit, C. O., 2007, "Effect of Fuel/Air Mixing on NOx Emissions and Stability in a Gas Premixed Combustion System," AIAA Paper No. 2007-1417.

[17] Khalil, S., Hourigan, K., and Thompson, M. C., 2006, "Response of Unconfined Vortex Breakdown to Axial Pulsing," Phys. Fluids, **18**, p. 038102.

[18] Sattelmayer, T., Felchlin, M. P., Haumann, J., Hellat, J., and Styner, D., 1990, "Second Generation Low-Emissions ABB Combustors for Gas Turbines: Burner Development and Tests at Atmospheric Pressure," ASME Paper No. 1990-GT-192.

[19] Döbbeling, K., Knopfle, H. P., and Polifke, W., 1994, "Low NOx Combustion of MBTU Fuels Using the ABB Double Cone Burner (EV Burner)," ASME Paper No. 94-GT-394.

[20] Matsumura, M., and Antonia, R. A., 1993, "Momentum and Heat Transport in the Turbulent Intermediate Wake of a Circular Cylinder," J. Fluid Mech., **250**, pp. 651–666.

[21] Wernert, P., and Favier, D., 1999, "Considerations About the Phase Averaging Method With Application to ELDV and PIV Measurements Over Pitching Airfoils," Exp. Fluids, **27**, pp. 473–483.

[22] Sonnenberger, R., Graichen, K., and Erk, P., 2000, "Fourier Averaging: A Phase-Averaging Method for Periodic Flow," Exp. Fluids, **28**, pp. 217–222.

[23] Holmes, P., Lumley, J., and Berkooz, G., 1998, *Turbulence, Coherent Structures, Dynamical Systems and Symmetry*, Cambridge University Press, Cambridge, England.

[24] Gallaire, F., and Chomaz, J. M., 2003, "Mode Selection in Swirling Jet Experiments: A Linear Stability Analysis," J. Fluid Mech., **494**, pp. 223–253.

[25] Roessler, M., 2006, "Experimentelle Bestimmung des Akustisch Angeregten Strömungsfeldes an Einem Drall-Brennermodell für Industrielle Gasturbinen," Studienarbeit, Technische Universität Berlin.

[26] Keller, J. J., Sattelmayer, T., and Thüringer, F., 1991, "Double Cone Burner for Gas Turbine Type 9 Retrofit Application," *Proceedings of the CIMAC 19th International Congress on Combustion Engines*, Florence, Italy.

[27] Flohr, P., Schmitt, P., and Paschereit, C. O., 2002, "Mixing Field Analysis of a Gas Turbine Burner," Paper No. IMECE 2002-39317.

[28] Li, F., Banaszuk, A., Tadmor, G., Noack, B. R., and Mehta, P. G., 2006, "A Reduced Order Galerkin Model for the Reacting Bluff Body Flame Holder," AIAA Paper No. 2006-3487.